Triphilic Organochalcogen Compounds for High-Capacity and Stable Solid-State Lithium–Sulfur Batteries†

Daiwei Wang,[b] Mitsutoshi Otaki,[b] Atif S. Alzahrani,[b,c] Yue Gao,[d] Jennifer L. Gray,[e] Qian Lu,[f] Meng Liao,[b] Timothy S. Arthur,[g] Donghai Wang*[a,b]

[a]*Department of Mechanical Engineering, Southern Methodist University, Dallas, TX 75205, USA. E-mail: donghaiwang@smu.edu*

[b]*Department of Mechanical Engineering, The Pennsylvania State University, University Park, PA 16801, USA.*

[c]*Interdisciplinary Research Center for Sustainable Energy Systems (IRC-SES), King Fahd University of Petroleum & Minerals (KFUPM), Dhahran 31261, Saudi Arabia*

[d]*Department of Chemistry, The Pennsylvania State University, University Park, PA 16801, USA.*

[e]*Materials Research Institute, The Pennsylvania State University, University Park, PA 16801, USA.*

[f]*Department of Chemical Engineering, The Pennsylvania State University, University Park, PA 16801, USA.*

[g]*Toyota Research Institute of North America, Ann Arbor, Michigan 48105, USA*

*Corresponding author

Supplementary Figures

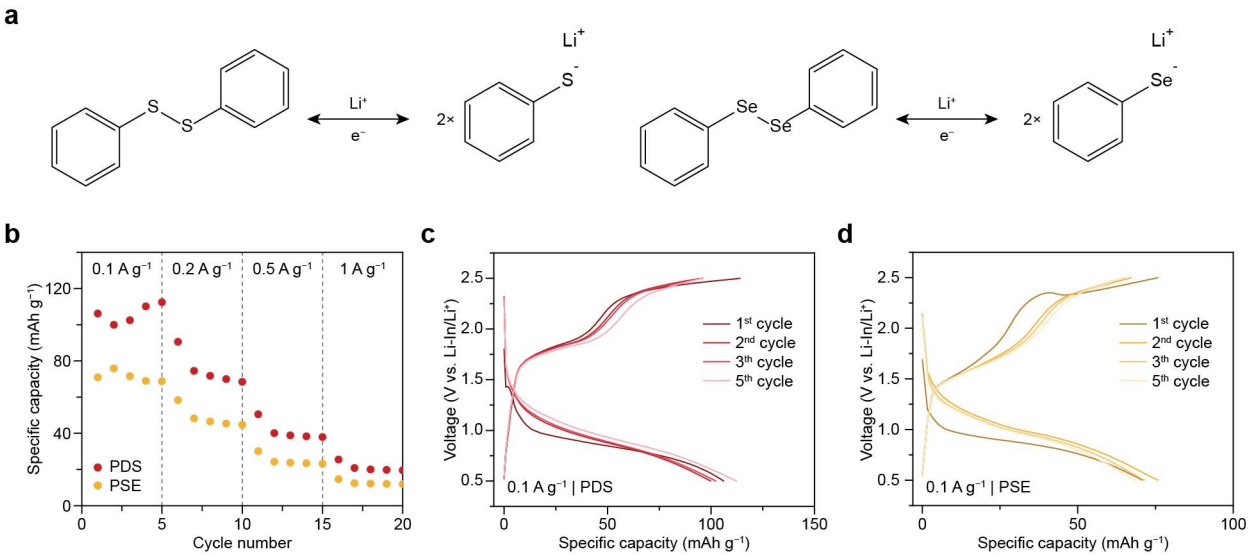

Fig. S1 (**a**) Redox reactions of phenyl disulfide (PDS) and phenyl diselenide (PSE) during lithiation/delithiation. (**b**) Rate performance of Li-In||PDS (Carbon/PDS/LPS=10/30/40, w/w/w, $75Li_2S{\cdot}25P_2S_5$ denoted as LPS) and Li-In||PSE (Carbon/PSE/LPS=10/45/40, w/w/w) cells and (**c,d**) the corresponding galvanostatic discharge-charge voltage profiles of the PDS (c) and PSE cathodes (d) at the 1st, 2nd, 3rd, and 5th cycle. The areal loadings of PDS and PSE cathode are ~1.8 mg cm^{-2}. During the charging process, two plateaus were observed. The lower-potential plateau is attributed to the formation of -S–S-/-Se–Se- bonds in PDS/PSE, while the higher-potential plateau at the (~2.3 V vs. Li-In/Li^+) corresponds to the oxidation of LPS.[1,2]

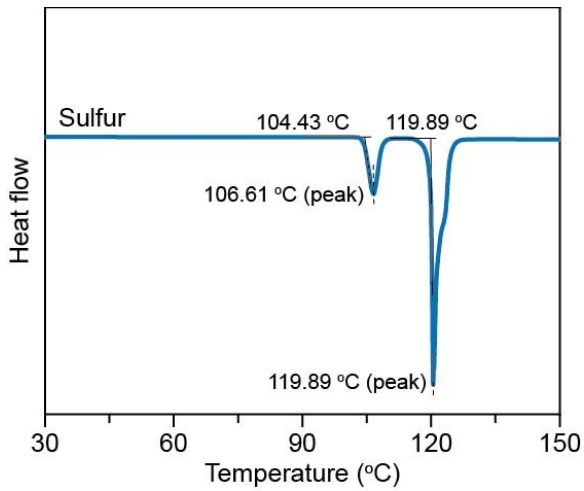

Fig. S2 Differential scanning calorimetry (DSC) curve of pure sulfur.

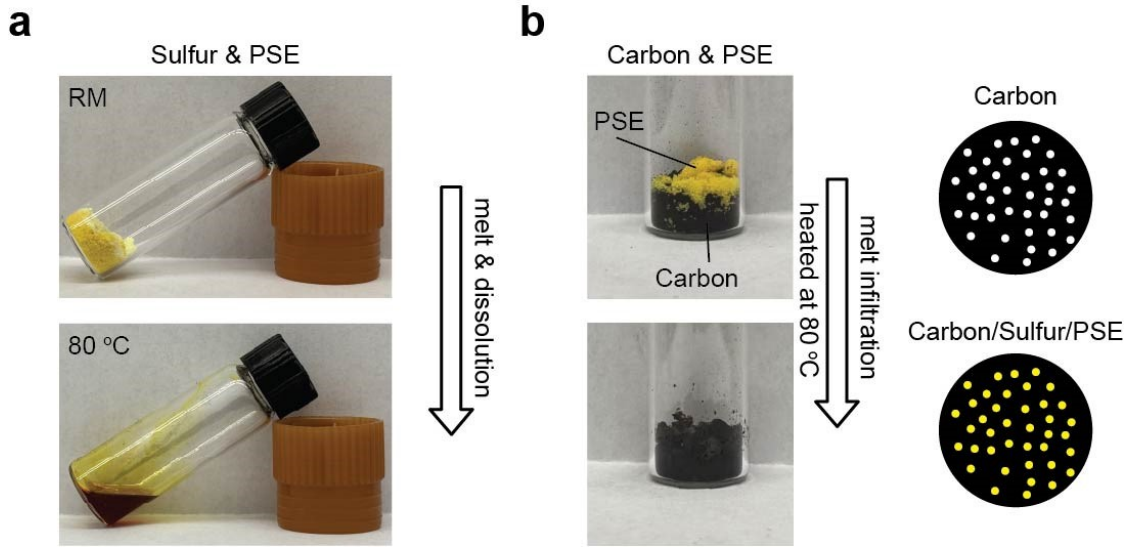

Fig. S3 (**a**) Photographs of the sulfur-PSE mixture before and after melting at 80 °C. (**b**) Photographs of the carbon-PSE mixture before and after melt infiltration (heat treatment at 80 °C), along with a schematic illustration depicting the infiltration of PSE-sulfur into the pores of porous carbon.

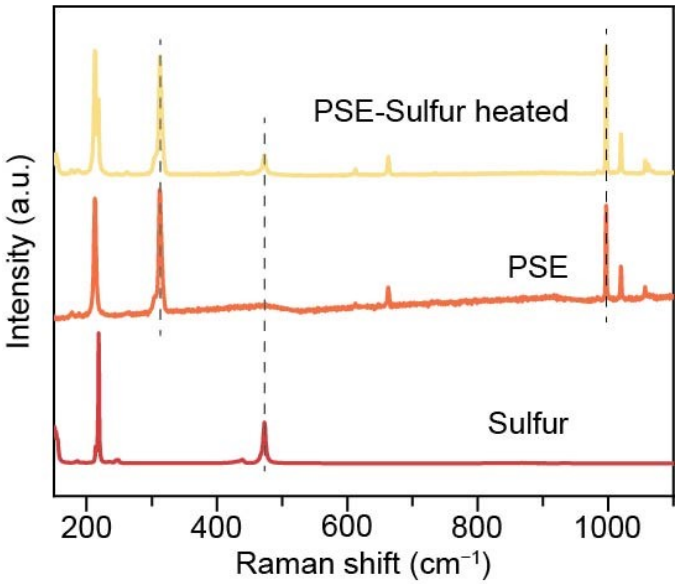

Fig. S4 Raman spectra of the heated PSE-sulfur mixture (after heat treatment at 80 °C), PSE, and sulfur. The results demonstrate that sulfur and PSE in the mixture maintain their pristine structure after heat treatment.

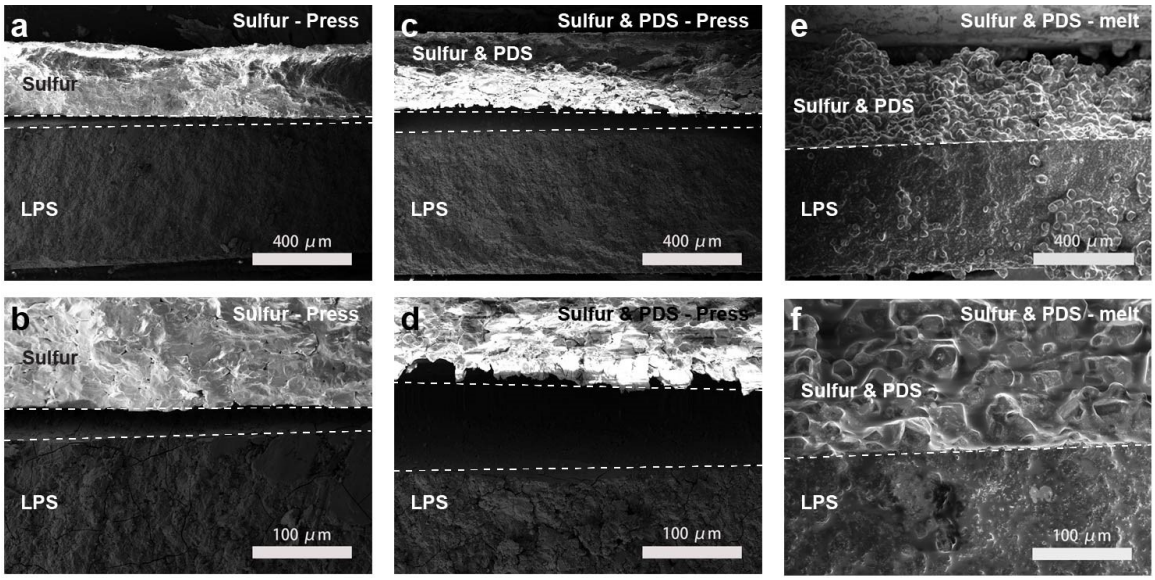

Fig. S5 Cross-sectional scanning electron microscope (SEM) images of the pellets formed by (**a,b**) pressing sulfur and LPS, (**c,d**) pressing sulfur-PDS mixture and LPS, and (**e,f**) pressing sulfur-PDS mixture and LPS followed by heat treatment at 80°C.

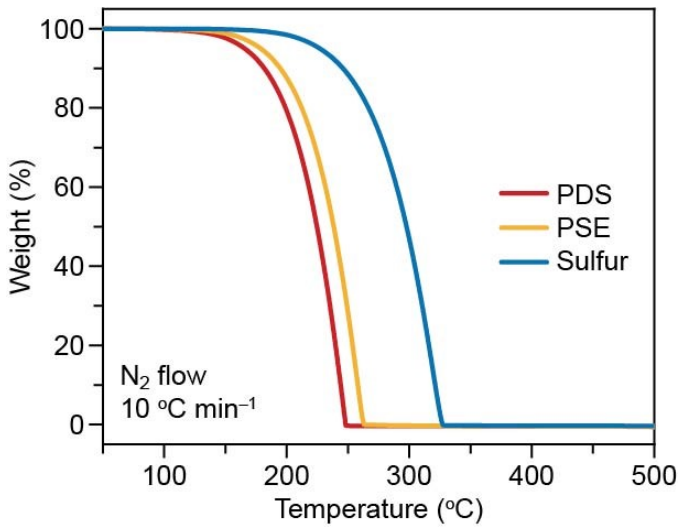

Fig. S6 Thermogravimetric analysis (TGA) curves of pure PDS, PSE, and sulfur.

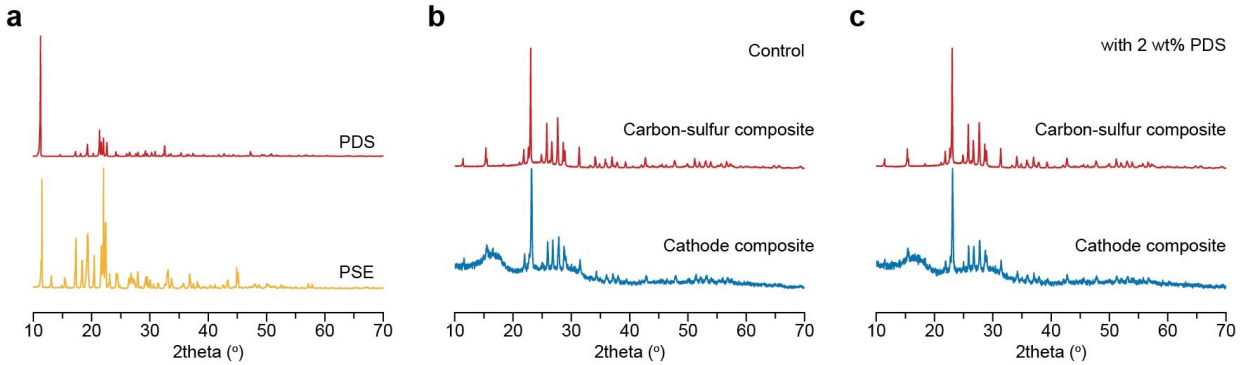

Fig. S7 X-ray diffraction (XRD) patterns of PDS, PSE, carbon-active material (AM) composites, and different cathodes.

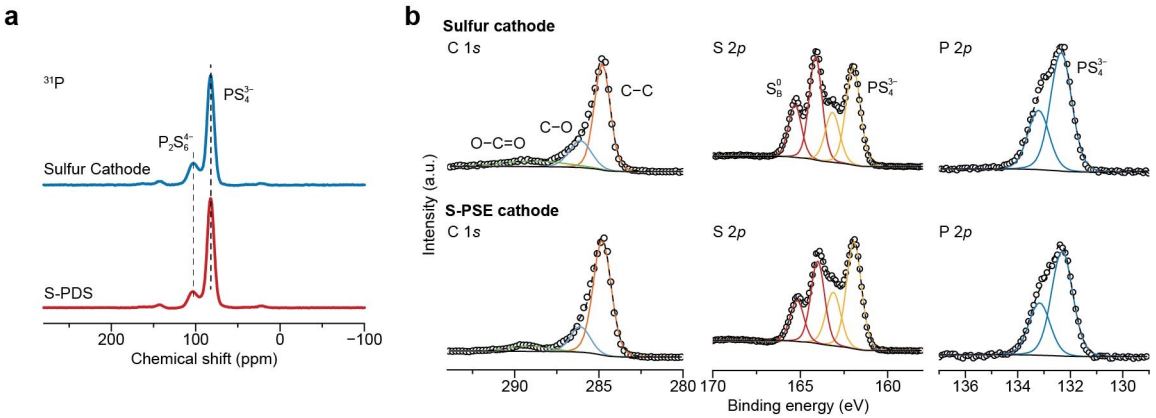

Fig. S8 (**a**) ^{31}P magic-angle spinning (MAS) nuclear magnetic resonance (NMR) spectra of the S-PDS and the control sulfur cathode powders. (**b**) High-resolution C 1*s*, S 2*p*, and P 2*p* X-ray photoelectron spectroscopy (XPS) spectra of the pristine control sulfur cathode and the S-PSE cathode surface.

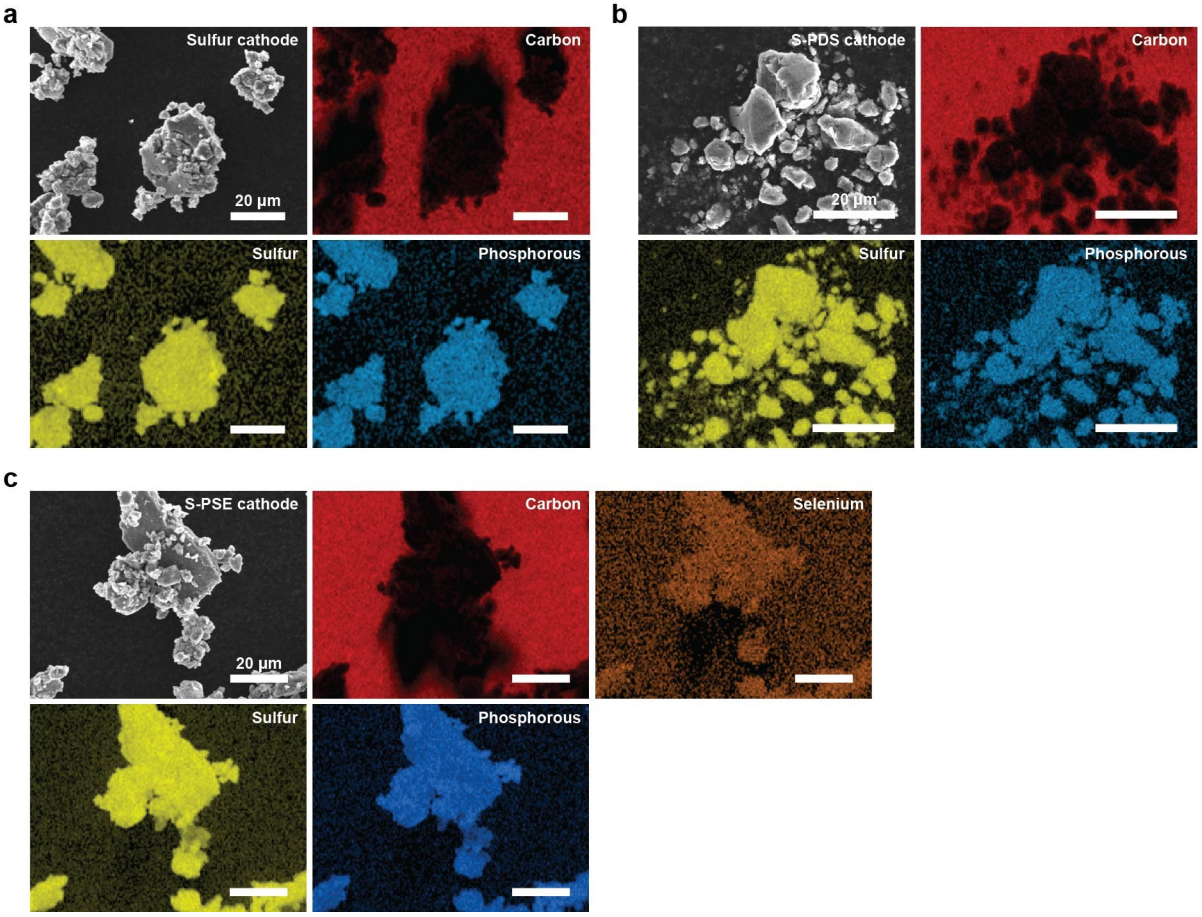

Fig. S9 SEM and energy dispersive spectroscopy (EDS) mapping of (**a**) the sulfur cathode, (**b**) the S-PDS cathode, and (**c**) the S-PSE cathode powders.

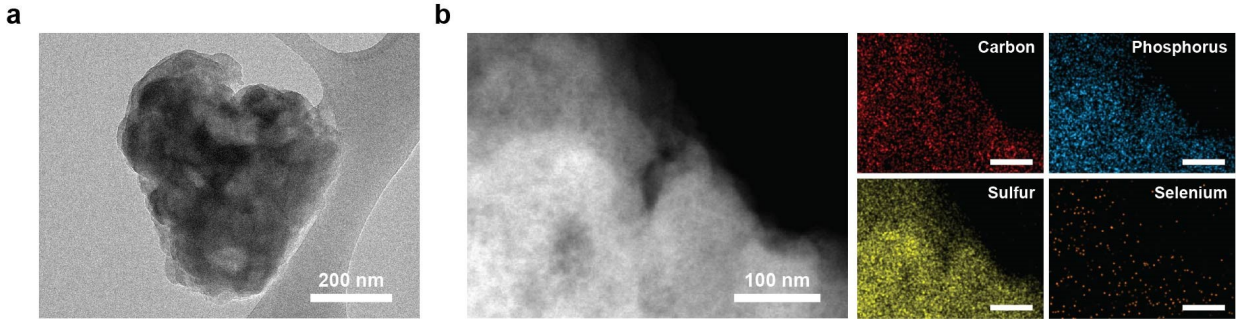

Fig. S10 (**a**) Cryogenic transmission electron microscope (Cryo-TEM) image of an S-PSE cathode powder. (**b**) Transmission electron microscope (STEM) and EDS mapping images of an S-PSE cathode particle, which show the relatively uniform distribution of all elements.

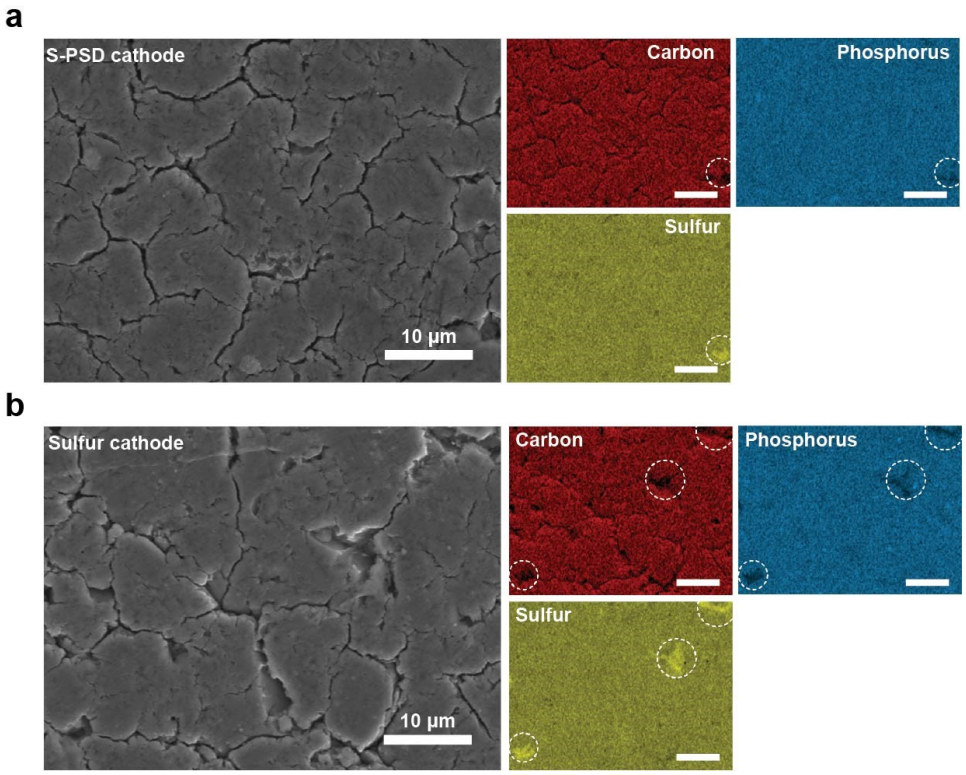

Fig. S11 SEM and EDS mapping images of the top surface of (**a**) the S-PDS cathode and (**b**) the sulfur cathode.

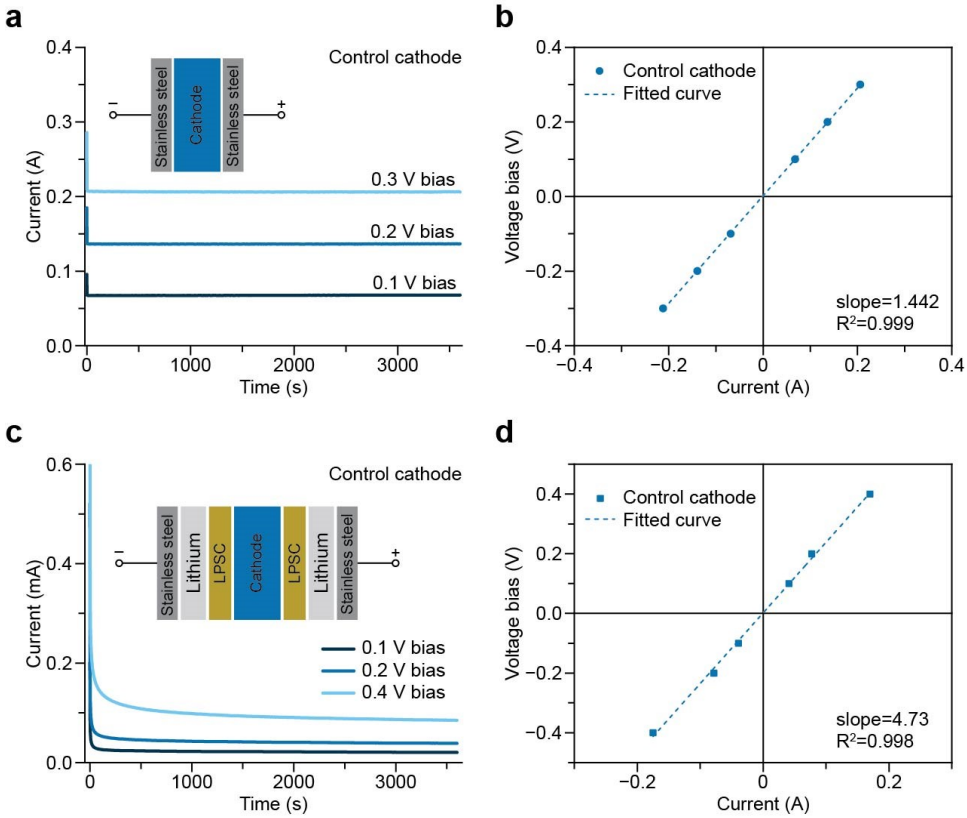

Fig. S12 Measurement of electronic and ionic conductivity of cathode composites via the d.c. polarization method at 30 °C. (**a**) Current-time curves of symmetric steel|cathode|steel cells under different voltage bias for electronic conductivity measurement. (**b**) Calculation of the electric resistance using voltage and equilibrated current (after 3600 s) via Ohm's law. (**c**) The current-time curves of symmetric steel|Li|LPSC|cathode|LPSC|Li|steel cells under different voltage biases for ionic conductivity measurement. (**d**) Calculation of the ionic resistance using voltage and equilibrated (after 3600 s) via Ohm's law.

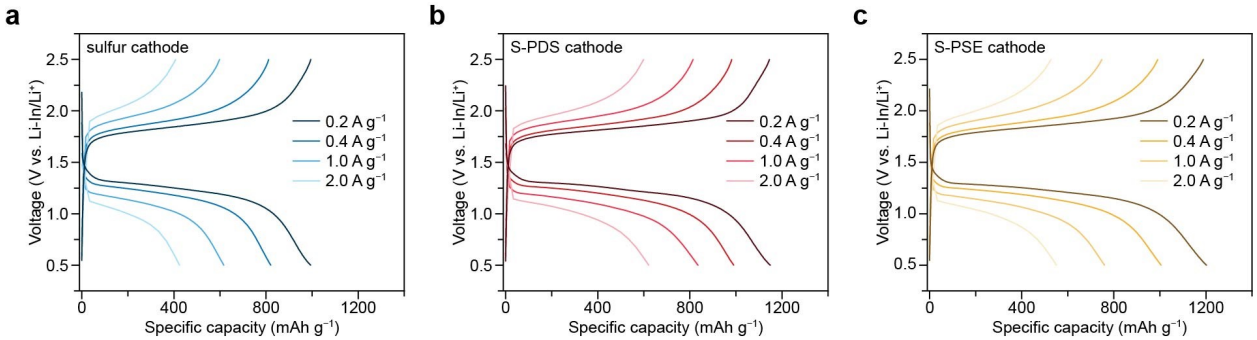

Fig. S13 Galvanostatic discharge-charge voltage profiles of (**a**) the sulfur cathode, (**b**) the S-PDS cathode, and (**c**) the S-PSE cathode at different current rates.

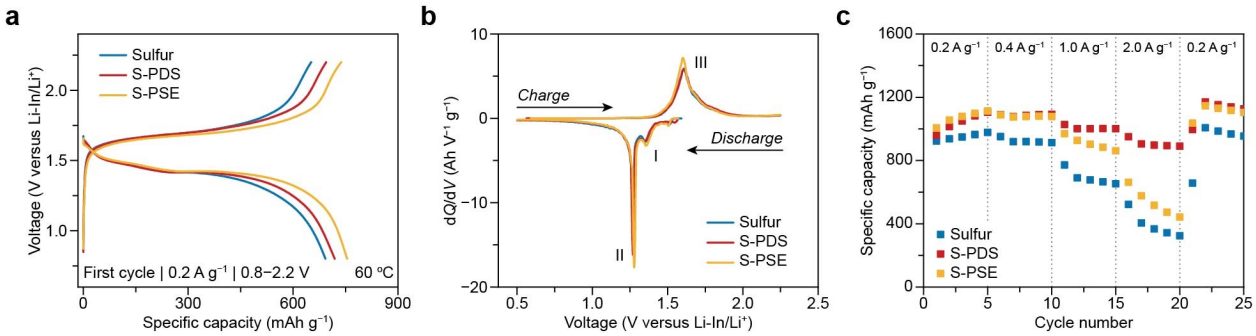

Fig. S14 Electrochemical evaluation of lithium–sulfur all-solid-state batteries (Li–S ASSBs) at 60 °C. (**a**) The galvanostatic discharge-charge curve of different cathodes at the initial cycle and (**b**) corresponding differential capacity (dQ/dV) curves. (**c**) Rate capability of different cathodes.

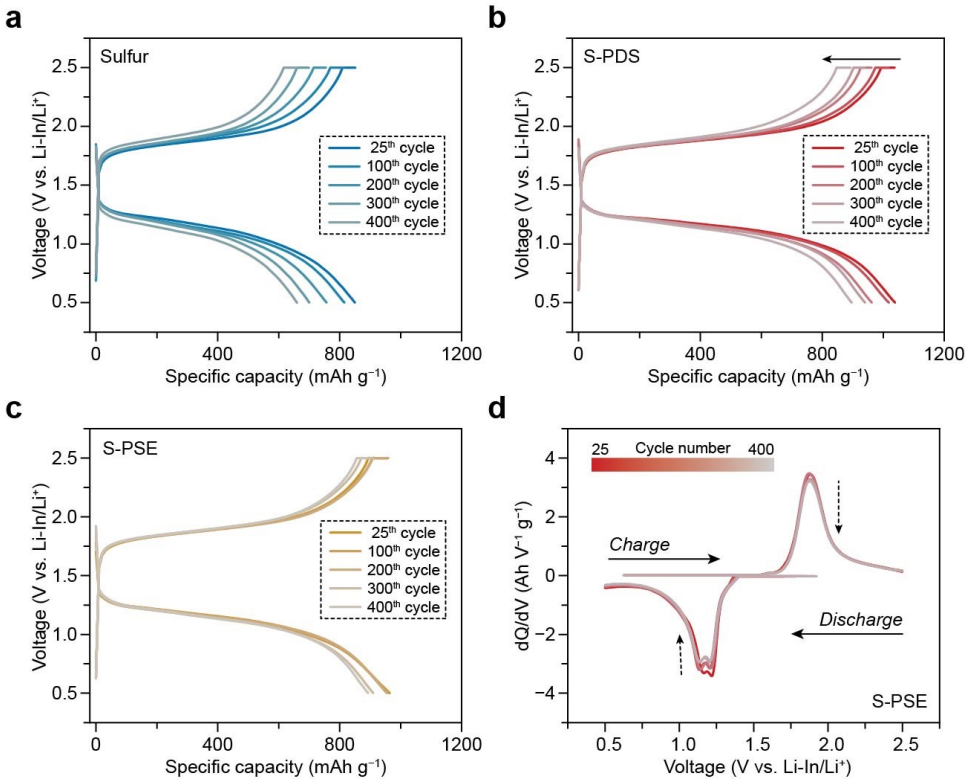

Fig. 15 Discharge-charge voltage profiles of (**a**) the S-PDS cathode, (**b**) the sulfur cathode, and (**c**) the S-PSE cathode at different cycles, corresponding to the cell cycling performance in Fig. 3d. (**d**) Differential capacity (dQ/dV) curves of the S-PSE cathode at different cycles (corresponding to the data in Fig. 3d).

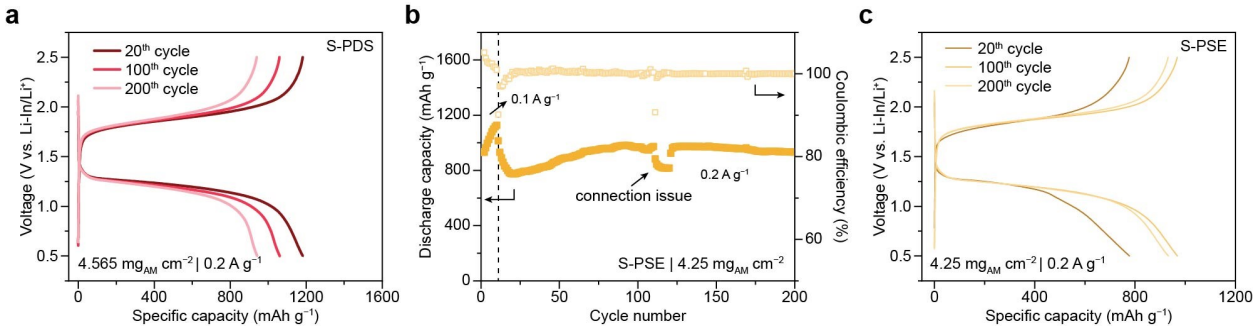

Fig. S16 (**a**) Discharge-charge voltage profiles the S-PDS cathode at different cycles, corresponding to the cell cycling performance in Fig. 3g. (**b**) Cycling performance of the S-PSE cathode with an areal AM loading of 4.25 mg cm^{-2} and (**c**) corresponding voltage profiles at different cycles.

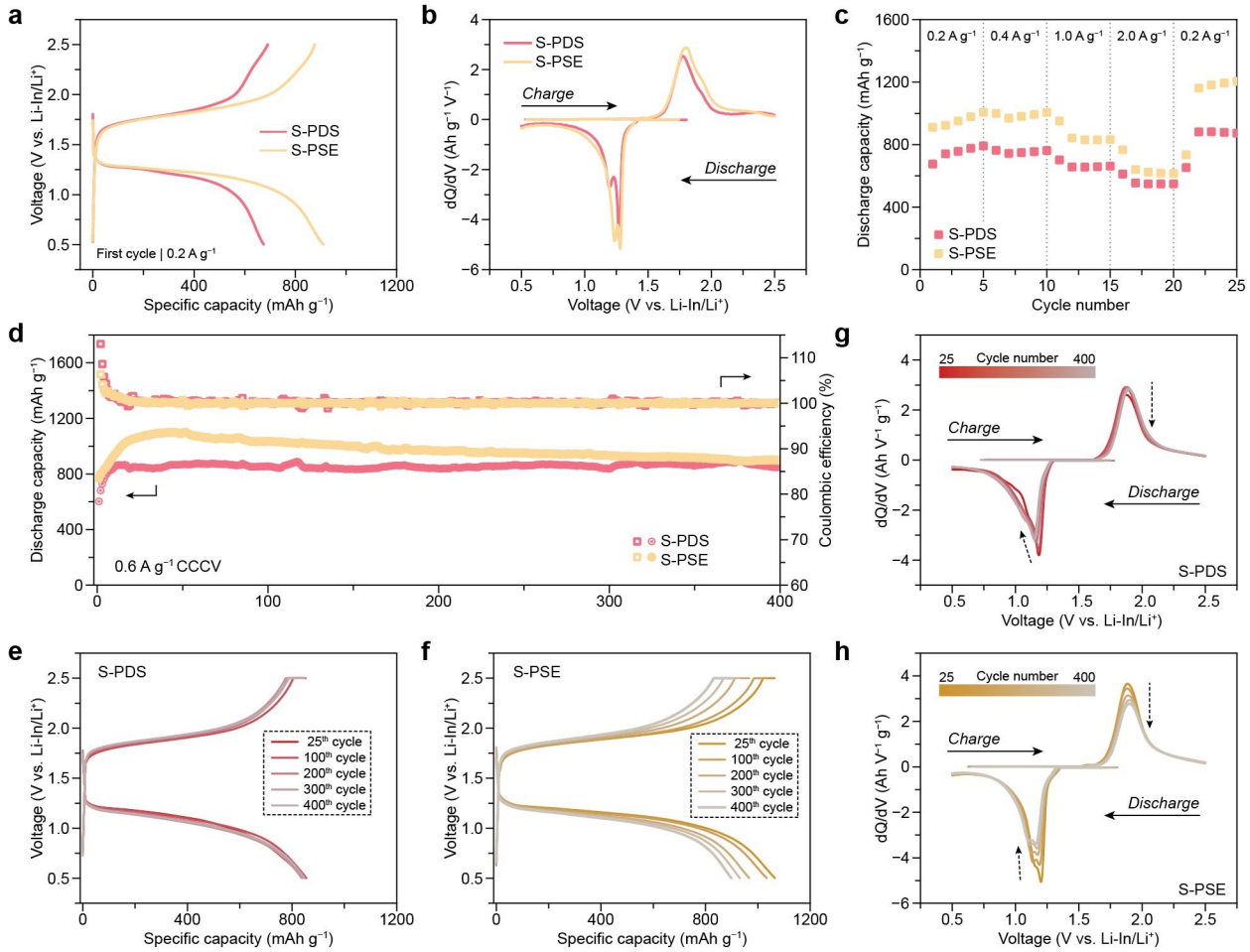

Fig. S17 Electrochemical evaluation of Li–S ASSBs using cathodes with 5 wt% PSD/PSE (carbon/sulfur/LPS/PDS or PSE=10/45/40/5, w/w/w/w) at room temperature. (**a**) The galvanostatic discharge-charge curve of different cathodes at the initial cycle and (**b**) corresponding dQ/dV curves. (**c**) Rate capability of different cathodes. (**d**) Cycling performance of different cathodes at 0.6 A g^{-1}_{AM} under CCCV mode with a cutoff current of 0.2 A g^{-1}_{AM} at 2.5 V. The areal AM loading is 1.7–2.1 mg cm^{-2}. (**e–h**) Corresponding (e,f) voltage profiles and (g,h) dQ/dV curves of (e,g) the S-PDS cathode and (f,h) the S-PDS cathode at different cycles.

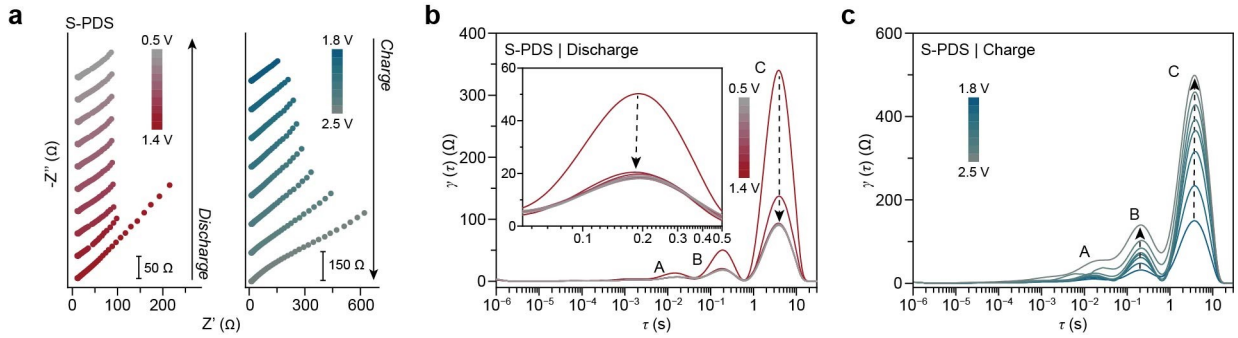

Fig. S18 (**a**) Impedance spectra of the cell with the S-PDS cathode at different potentials during the first discharge/charge cycle (cycled at 0.2 A g^{-1}_{AM} and rested for 20 mins before each measurement). (**b**,**c**) Corresponding distribution of relaxation times (DRT) analysis of the impedance spectra during the discharge (**b**) and charge process (**c**).

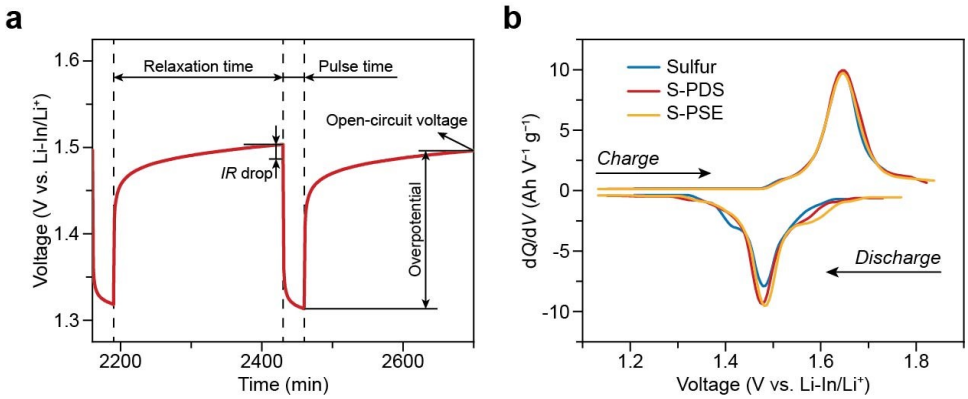

Fig. S19 Galvanostatic intermittent titration technique (GITT) analysis. (**a**) GITT curves at the selected steps during discharge. (**b**) Differential capacity (dQ/dV) curves derived from the open-circuit curves.

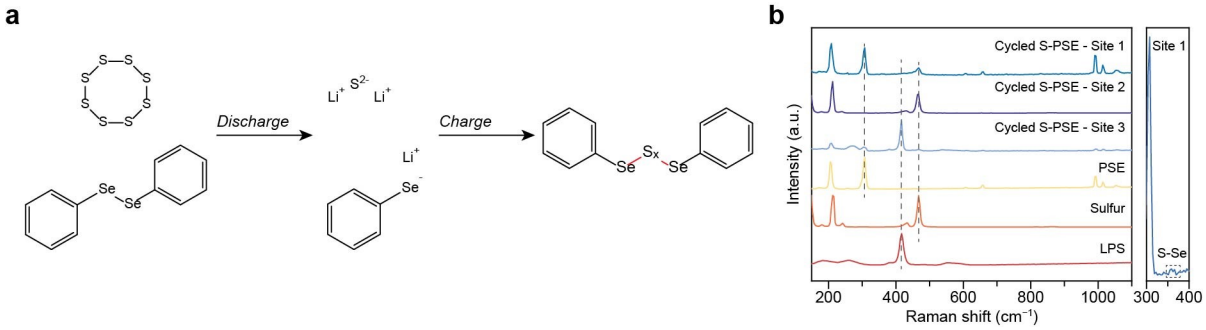

Fig. S20 (**a**) Schematic illustration of the electrochemical redox mechanism in S-PSE electrodes. (**b**) Raman spectra of LPS, sulfur, PSE, and the cycled S-PSE electrode at the charging state (S/PSE/Carbon/LPS=20/25/10/40, w/w/w/w).

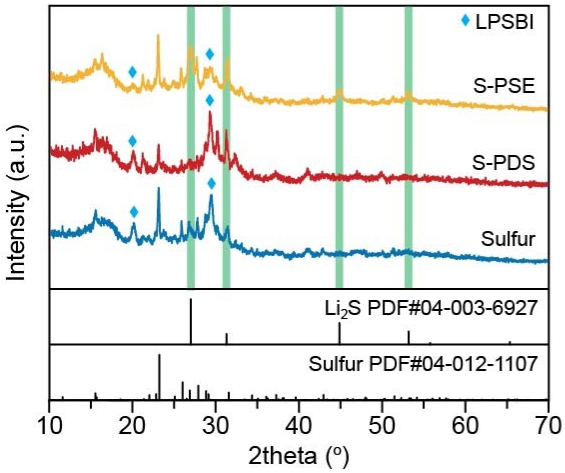

Fig. S21 XRD patterns of the cycled batteries with the sulfur cathode (the 715th cycle), the S-PDS cathode (the 500th cycle), and the S-PSE cathode (the 549th cycle) at the charged state.

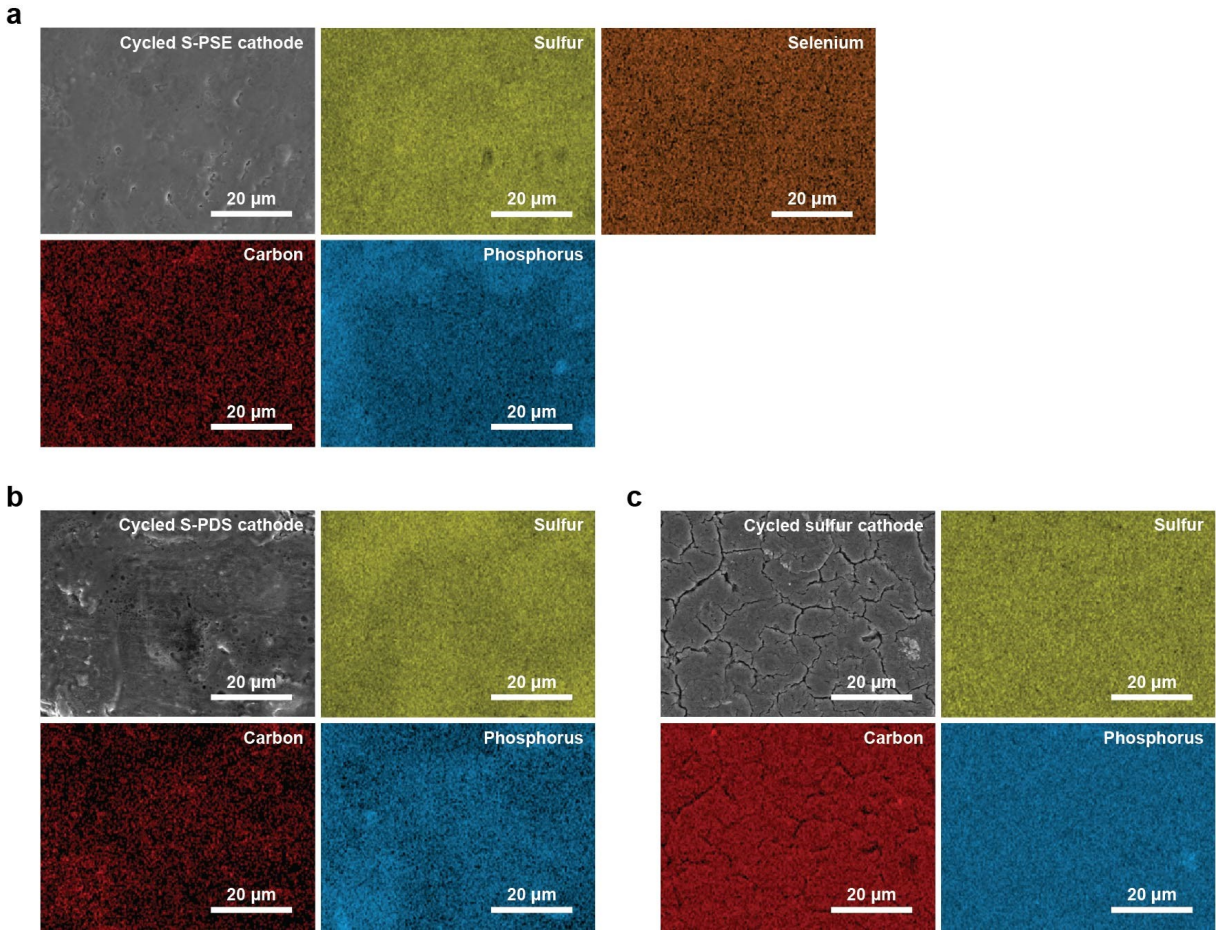

Fig. S22 SEM and EDS mapping images of (**a**) the S-PSE cathode, (**b**) the S-PDS cathode, and (**c**) the cycled sulfur cathode at the charged state.

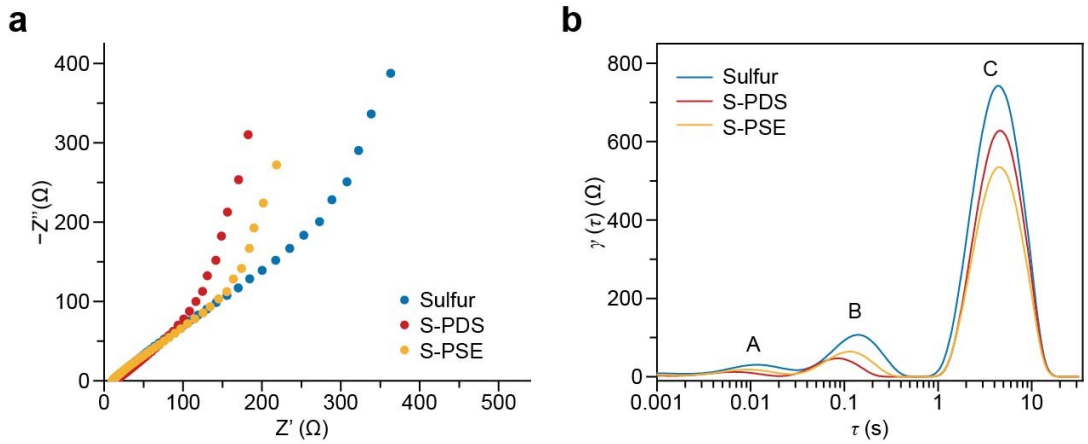

Fig. S23 (**a**) Impedance spectra of the cycled batteries with different cathodes and (**b**) corresponding DRT curves.

Supporting Tables

Table S1 Potentials of redox reaction peaks in the differential capacity curves.

Cathode	Discharge-Peak I (V)		Discharge-Peak II (V)		Charge-Peak III (V)	
	vs. Li-In/Li^+	vs. Li/Li^+	vs. Li-In/Li^+	vs. Li/Li^+	vs. Li-In/Li^+	vs. Li/Li^+
Sulfur	1.295	1.915	1.218	1.838	1.801	2.421
S-2PDS	1.305	1.925	1.228	1.848	1.783	2.393
S-2PSE	1.298	1.918	1.239	1.859	1.798	2.418

Table S2 Room-temperature electrochemical performance comparison with results reported in the literature.

No.	Methods	ω_{AM} a) (wt%)	m_{AM} b) (mg/cm^2)	I c) (A/g$_{AM}$)	Q d) (mAh/g$_{AM}$)	e e) (Wh/kg$_{AM}$)	Voltage window (V vs. Li/Li$^+$)	Cycle number	Fading rate f) (% per cycle)	Refs
1	Interface	20	2.0	0.0825	1700	612	1.42–3.12	n/a	n/a	3
			4.0	0.0825	1600	576		250	0.144	
2	Interface	25	1.3	0.1675	1138.7	512.4	1.42–2.82	200	0.062	4
3	Solid Electrolyte	33	3.0	0.1309	1483	880.9	1.62–3.02	n/a	n/a	5
			5.0	0.0785	1432	850.6		50	0.330	
4	Conductive Host	28	1.7	0.335	1467	739.4	1.20–3.00	300	0.039	6
5	Sulfur Engineering	40	1.6	0.05	930	669.6	1.50–3.00	50	0.313	7
6	Sulfur-Metal Sulfides	60 (S/VS_2=1/2)	1.7	0.071	640	691.2	1.42–3.12	50	n/a	8
			1.9	0.142 m) 0.068 n)	579	625.3		200	n/a	
7	Sulfur-Metal Sulfides	30 (S/FeS_2=1/1)	1.0	0.0835	1200	698.4	1.30–3.10	20	none	9
8	Organic-Inorganic Sulfur Hybrid	50 (S/PDS=48/2)	2.35	0.2	1149.2	1022.3	1.12–3.12	n/a	n/a	This Work
			1.595	0.6	1063.2	903.8		400	0.044	
			4.565	0.2	1184	1045.9		200	0.115	
		50 (S/PSE=48/2)	1.78	0.2	1202.6	1059.5		n/a	n/a	
			1.705	0.6	999.8	847.5		400	0.047	
			4.25	0.2	981.6	852.8		200	0.028	

a) weight percentage of the active material in the cathode; b) areal active material loading; c) current rate; d) discharge capacity; e) gravimetric energy density (calculated based on the actual average voltage vs. Li/Li$^+$, if available, or using a standard average voltage of 1.8 V vs. Li/Li$^+$); f)the fading rate is calculated based on the maximum discharge capacity achieved (if available); m) the current rate applied from the 1st cycle to the 100th cycles; n) the current rate applied from the 101st cycle to the 200th cycle.

Table S3 Summary of theoretical capacity and active material utilization of different cathodes.

Cathode Composition	Theoretical capacity (mAh g^{-1})	Discharge capacity (mAh g^{-1}_{AM} at 0.2 A g^{-1}_{AM})	AM Utilization (%)
Pure Sulfur	1675.0	994.0	59.3
Sulfur/PDS=48/2	1617.8	1149.2	71.0
Sulfur/PSE=48/2	1614.8	1202.6	74.5
Sulfur/PDS=45/5	1532.0	882.4	57.6
Sulfur/PSE=45/5	1524.6	1181.4	77.5

References

1 H. Gamo, K. Hikima, A. Matsuda, *Chem. Mater.* 2022, **34**, 10952–10963.
2 T. Hakari, M. Deguchi, K. Mitsuhara, T. Ohta, K. Saito, Y. Orikasa, Y. Uchimoto, Y. Kowada, A. Hayashi, M. Tatsumisago, *Chem. Mater.* 2017, **34**, 4768–4774.
3 H. Kim, H.-N. Choi, J.-Y. Hwang, C. S. Yoon, Y.-K. Sun, *ACS Energy Lett.* 2023, **8**, 3971–3979.
4 L.-P. Hou, H. Yuan, C.-Z. Zhao, L. Xu, G.-L. Zhu, H.-X. Nan, X.-B. Cheng, Q.-B. Liu, C.-X. He, J.-Q. Huang, Q. Zhang, *Energy Storage Mater.* 2020, **25**, 436–442.
5 H. Guo, J. Li, M. Burton, J. Cattermull, Y. Liang, Y. Chart, G. J. Rees, J. Aspinall, M. Pasta, *Cell Rep. Phys. Sci.* 2024, **5**, 102228.
6 T. Jin, K. Liang, J.-H. Yu, T. Wang, Y. Li, T.-D. Li, S. P. Ong, J.-S. Yu, Y. Yang, *Nano Lett.* 2024, **24**, 6625–6633.
7 X. Li, J. Liang, J. Luo, C. Wang, X. Li, Q. Sun, R. Li, L. Zhang, R. Yang, S. Lu, H. Huang, X. Sun, *Adv. Mater.* 2019, **31**, 1808100.
8 S. Xu, C. Y. Kwok, L. Zhou, Z. Zhang, I. Kochetkov, L. F. Nazar, *Adv. Funct. Mater.* 2021, **31**, 2004239.
9 U. Ulissi, S. Ito, S. M. Hosseini, A. Varzi, Y. Aihara, S. Passerini, *Adv. Energy Mater.* 2018, **8**, 1801462.